

Finding Chairs in Indoor Scenes under Heavy Occlusion using Scene Statistics

Moos Hueting
University College London
m.hueting@ucl.ac.uk

Vladimir Kim
Adobe Systems
San Jose
vokim@adobe.com

Ersin Yumer
Adobe Systems
San Jose
yumer@adobe.com

Nathan Carr
Adobe Systems
San Jose
ncarr@adobe.com

Niloy Mitra
University College London
n.mittra@ucl.ac.uk

Abstract

3D geometry mockups of single images of indoor scenes are useful for many purposes including interior design, content creation for virtual reality and image manipulation. Unfortunately, modeling a scene from an image by hand requires expert knowledge and is time-consuming. We aim to construct scene mockups from single images automatically. However, automatically inferring 3D scenes from 2D images is an ill-posed problem, as 2D images are projections of many meaningful attributes (e.g. lighting, material, form), with objects regularly being occluded by themselves or others. Performance of recent advances in scene mockup generation mirror this observation, and work mostly on fully visible objects. To improve beyond this baseline we need to take into account contextual information, exploiting the fact that objects co-occur mostly in highly regular configurations. We exploit this regularity in the form of prior information. Specifically, we first use a neural network to extract keypoints, then feed these keypoints to a candidate object generation stage. From these candidates, an optimal selection is then made using pairwise co-occurrence statistics, gleaned from a database of 3D scenes. This process is iterated, allowing for candidates with low keypoint response to be detected based on the location of neighbouring objects. We demonstrate that our pipeline outperforms combinations of state-of-the-art single object methods, especially for scenes with severely occluded objects. All code, training data and scene statistics are released for the benefit of the community.

1. Introduction

Large sets of 3D indoor scenes are useful for purposes ranging from architecture and product design to virtual reality content and game asset creation. Aside from being

used directly as a resource for rendering or interactive purposes, statistics extracted from them can be used to gain insight into how objects are commonly used, and how they are commonly placed with respect to each other. However, such sets are unfortunately hard to come by and expensive to manually create. In contrast, 2D photographs of such indoor scenes are widely and freely available, as are large databases of individual 3D models. It makes sense, then, to try and convert 2D photographs to 3D scenes making use of 3D models. This gives rise to an essential problem in computer vision and graphics, which we will henceforth call the *mockup problem*: given a single 2D photograph and a database of 3D models, place instances from this database into a 3D scene as to reconstruct the photograph as accurately as possible.

The problem is inherently ill-posed, as photographs are the result of the projection of many complex attributes (e.g. geometry, material, illumination). Indeed, we are faced with reconstructing an entire dimension that was lost when the photograph was taken. Additionally, inter- and intra-object occlusions limit the amount of visual information available for certain objects, making the reconstruction process more difficult still. It is possible for computer vision algorithms to make reasonable inferences from a single natural image by relying on relevant *prior knowledge* about the image in question. Even so, the complexity of the problem, together with the difficulty of gathering large amounts of training data, makes the mockup problem a highly challenging one.

Recent advances have addressed parts of the goal by looking at simpler problems, such as object recognition [10], localization [19], and pose prediction [23]. Unfortunately, these techniques are designed for objects that are almost fully visible, and fail under moderate to severe occlusions, making them useful only for the simplest of scenes. Moreover, they work on a single object basis,



Figure 1: The chair marked in blue can easily be distinguished as being a chair through its context, even though most of the object is occluded.

discarding any more high-level information that might be present. Simply combining these methods thus yields limited success (see Section 5).

In this paper, we suggest that in order to improve beyond this baseline, we need to reason about the scene on a more global basis, and inject deeper knowledge of the domain into the optimization process. Our key insight is that scenes typically exhibit significant regularity in terms of co-occurrence of objects, which can be exploited as explicit prior information to make predictions about object identity, placement and orientation, even when such objects are in highly occluded regions, and thus single-object based methods fail.

Intuitively, this approach makes sense – it matches the way we as humans reason under similar noisy conditions. A heavily occluded chair is still easily distinguishable as such due to the presence of other chairs and a table (see Figure 1), as we have a good understanding of typical chair-table arrangements. By explicitly modeling this type of knowledge, we can find placements that would otherwise carry too little visual information for accurate recognition.

This insight is captured in our method by combining reprojection error of known keypoints with pairwise object co-occurrence costs in the objective function. Candidate placements are generated and tested on the one hand based on semantic keypoint maps from a newly trained deep neural network, and on the other hand based on the pairwise agreement between instances according to a model of object co-occurrence statistics, gleaned from a database of pre-existing 3D scenes.

We tested our approach quantitatively on 100 hand-annotated images and show a marked improvement of recognition over baseline methods. Although our current

implementation is focused on the *chair* class, the method itself is not inherently limited to this, and could be extended to other classes with appropriate data annotation effort.

The contributions of this paper are:

- a keypoint estimation network for estimating relevant keypoints of multiple instances of chairs in a single image,
- a pairwise co-occurrence model capturing likelihood of co-occurring chair instances,
- an end-to-end pipeline for finding chairs in single images that beats the state-of-the-art,
- a ground-truth dataset of 100 scenes for testing performance of similar methods.

2. Related Work

Scene mockups Automatic scene mockup generation research is recently gaining acceleration, mainly due to the ubiquity of the new generation capture methods that enable partial 3D and/or depth capture. Mattausch et al. [16] used 3D point cloud input to identify repeated objects by clustering similar patches. Li et al. [14] utilize an RGB-D sensor to scan an environment in real time, and use the depth input to detect 3D objects queried from a database. Note that these works take 3D data as input, where we take a single 2D image.

Most recently, Izadinia et al. [13] demonstrated scene reconstruction with CAD models from a single image using image based object detection and pose estimation approaches. Although their objective is similar to ours, the performance is bounded by the individual vision algorithms utilized in their pipeline. For example, if the segmentation misses an object because of significant occlusion, there is no mechanism to recover it in the reconstruction. On the contrary, our novel pairwise based search incorporates high level relationships typical to indoor scenes to recover from such failures successfully.

3D to 2D alignment An important part of the scene mock up process involves the fine-pose alignment of a given 3D object to a 2D image. Lin et al. [15] approached the problem from a local image statistics perspective and used image-space features to align a given furniture model to a given image. Aubry et al. [5] utilized a discriminative visual element processing step for each shape in a 3D model database, which are then used to localize and align models to given 2D photographs of indoor scenes. Like most existing methods, their approach breaks down under significant occlusion. Our method is more robust in these cases, as other nearby objects can provide higher order information to fill in the lost information. We compare our method with Aubry

et al. as a baseline and show favourable results (see Section 5).

Scene priors for reconstruction. Scene arrangement priors have been successfully demonstrated in 3D reconstruction from unstructured 3D input, as well as scene synthesis [8]. Shao et al. [20] demonstrated that scenes with significant occlusion can be reconstructed from depth images by reasoning about the physical plausibility of object placements. Monszpart et al. [17] uses the insight that planar patches in indoor scenes are often oriented in a sparse set of directions to regularize the process of 3D reconstruction. On the other hand, based on priors between human Fisher et al. [9], leveraged human activity priors together with object relationships as a foundation for 3D scenes synthesis. In contrast to the complex and high order joint relationships used in these works, our object centric templates are compact and primarily encode the repetition of similar shapes (such as two side by side chairs) across pose and location. This compact and simple template representation help ensure our search is tractable at runtime.

3. Motivation and Overview

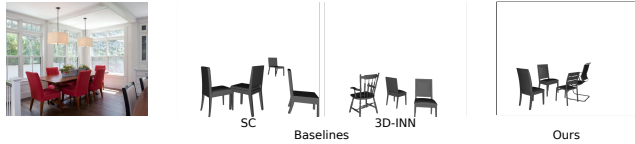


Figure 2: Methods based only on the image quickly fail in the presence of less than ideally visible chairs. Our method deals with this situation much better.

To understand the motivation for our approach, we will consider the problem from a high level. Summarily spoken, we are constructing a method that converts a 2D photograph to a 3D scene. The most straightforward and classical way of doing so would be to train some machine learning method on some feature representation of many examples of 2D photograph / 3D scene pairs and use the resulting classifier as our mockup black box. Such an approach can be easily constructed from a combination of existing methods. It turns out, however, that such methods fail badly when confronted with all but the simplest of scenes. In fact, in our evaluation (Section 5) we compare our method with two baselines that follow this approach. Foreshadowing some of their results in the left side of Figure 2 shows that chairs that are obviously visible get placed correctly, but any instances that are a little harder to see fail to be selected.

To understand this failure, and more importantly how to circumvent it, it is useful to consider how we as humans are capable of understanding these kind of scenes. Looking



Figure 3: As humans, our understanding of scenes is heavily predicated on the context. From left to right, less global information is available, making the classification of the marked object as “chair” harder

at Figure 3, we see a selection of chairs, some heavily occluded and some clearly visible, in 3 different conditions. In the first condition, we see the full scene, in the second only the local context and in the last condition we only see the pixels that belong to the chair itself. It is clear to see that for the recognition of the unoccluded chair the environment is not important – the shape of the object is clearly visible, and we immediately recognize the chair. However, in the heavily occluded case, the task of recognizing the chair becomes easier as more context gets added. For the last column, we might hypothesize that the image regions belong to a chair, but we have no way of confirming this for certain – unless the context is restored.

Clearly, the addition of context gives us extra information in classifying and posing the objects in a scene. But this is not the whole story. Importantly, the extra information we are given when seeing the entire image is only useful given prior knowledge we have built up over previous experiences. In this particular example, the added context helps us only because we know that chairs often occur together with other chairs and tables. Given this prior knowledge and the global context of the object, our recognition efficacy is enhanced.

This insight is what we capture in our approach to the scene mockup problem: to maximize performance on the mockup task, we need to consider both local information and the context the objects are placed in. Furthermore, to understand this context we need to tell the system what usual scenes look like.

We express these notions in our method as follows: we will extract *local* information from the input image using a keypoint detection network (Section 4.2), then *model* the prior knowledge about how scenes are usually built up (Section 4.4.1), finally combining this model with the keypoints to find chair instances from a *global* perspective (Section 4.4.2). This added high level information allows us to push performance past that of the previously mentioned approach of using only the input data itself (see Figure 2, right). In the next section, we will go through each of these

steps in detail.

4. Method

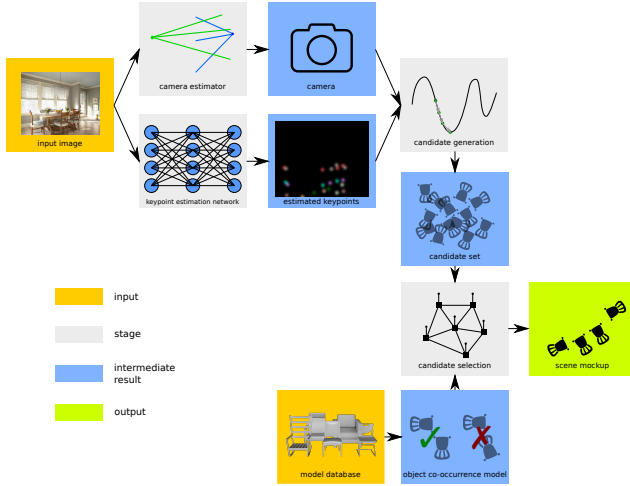


Figure 4: The full pipeline of our method.

Our pipeline (Figure 4) takes as input a photograph x and a database of 3D chair models M , and outputs a mocked up 3D scene S , such that the reprojection of S with the separately estimated camera C results in an image as similar as possible to x (see Figure 5).

As a preprocessing step, the scene camera C is estimated using an off-the-shelf technique ([11]), giving us focal length and camera orientation (Section 4.1). We then enter the main pipeline, which consists of three stages. In the first stage, the image is passed through a keypoint estimation network that outputs a set of *keypoint probability maps*, representing at each pixel the probability of the presence of a certain semantically meaningful keypoint (Section 4.2). In the second stage, these keypoint maps are combined with the estimated camera C to generate candidate object placements (Section 4.3). In the third stage, a selection is made among these candidates by optimizing an objective function which combines object-to-keypoint-map matching with pairwise placement agreement according to a pre-trained object co-occurrence model (Section 4.4). The second and third stages are then iterated, this time taking into account the previously found objects during candidate generation as a strong prior (Section 4.5). This process is iterated until convergence. We now discuss each of these stages in turn.

4.1. Camera estimation

To convert sets of 2D keypoints to possible 3D locations we need the intrinsic and extrinsic parameters of the camera with which photo x was taken. Specifically, for a good reconstruction, we need the orientation of the camera with

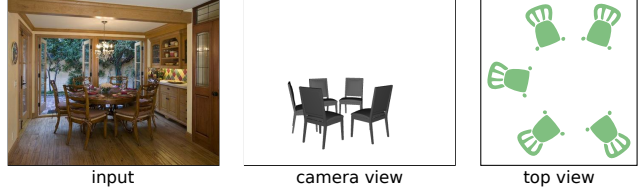


Figure 5: Intended working of our method: we take a single image of a structured indoor scene as input, and output a 3D scene with the constituent chairs recovered in the right location and pose, as well as the camera parameters that reproject this scene as close as possible to the original input.

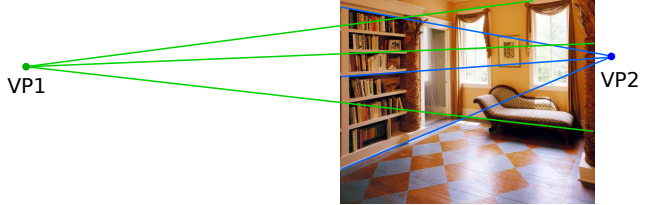


Figure 6: By estimating vanishing points in the image, the camera rotation matrix and focal length can be detected. Detecting scale a priori is not possible.

respect to the ground plane in the form of rotation matrix C_R , the focal length C_f , and a measure of the scale of the room C_s . However, estimating the scale of the room without prior information is not possible – even if we know the 2D location of a chair, it still might be 1 meter or 100 meters tall. There is no way of deciding this without some prior knowledge about chairs and their dimensions. We thus fix our scale parameter and only estimate C_f and C_R , and replace C_s with individual scale parameters for each object in the optimization later on. Most methods for camera parameter estimation indeed focus on C_f and C_r , and to do so rely on automatically estimating vanishing points (see Figure 6). We employ the method from Hedau et al. [11]. In summary, their method uses structured learning from Tsochantaridis et al. [21] to rank multiple room layout candidates, which are generated from estimated vanishing points. We refer to the paper from Hedau et al. for more information.

To complete our camera parameters, we pick meters as unit in our world coordinate system (the same coordinate system used by our model set), and set the camera's location C_t as being at eye height (1.8m) on world origin. This altogether yields our camera C .

4.2. Keypoint maps

Our goal is to find location and pose of as many chairs in the scene as possible. We aim to do this by finding all instances of a predefined set of semantically meaningful keypoints in the image, and then use the estimated camera together with a 3D chair template consisting of those

same keypoints to reconstruct the 3D location and pose of the chairs.

We start by defining a set of general keypoint types for the chair object class. Each keypoint type represents one or more keypoints that should be present in each (reasonable) chair instance. We selected 8 keypoint types, each of which is uniquely identifiable on every reasonable chair. These keypoint types are shown in Figure 7.



Figure 7: Selected keypoint types.

4.2.1 Keypoint location map

A keypoint location map is a 2D map whose domain is the input image x , and represents belief about the presence of a specific keypoint type at a specific pixel of x . It is represented as a $r \times r$ single-channel matrix, with values between 0 and 1. In the case of perfect information, the matrix will have value 0 everywhere except for those locations where a keypoint of the corresponding type is present, where it would have value 1. However, as we will employ an L2 loss function, such step-function keypoint maps would result in an extremely discontinuous error landscape, destabilizing the training process. Instead, we represent each keypoint using a Gaussian lobe centered around its true location, resulting in a much smoother loss function (see Figure 8).

4.2.2 Keypoint estimation network

To extract keypoint location maps for each keypoint type from an input image, we employ a deep learning architecture. This network takes our image x as input and outputs a

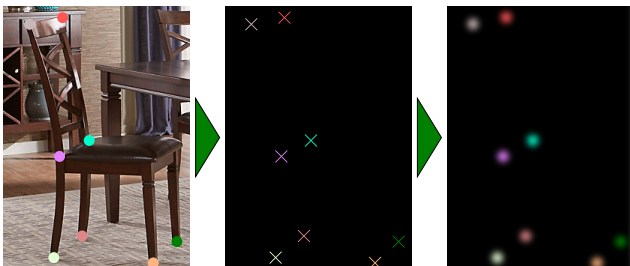


Figure 8: To facilitate the training process the keypoints are represented as Gaussian lobes around their location.

architecture	MSE
ResNet-50 [10]	3.24×10^{-5}
CPM [22]	1.02×10^{-4}

Table 1: Performance of the two tried architectures on our task. ResNet-50’s advantage of being pretrained on ImageNet gives it the edge over CPM.

set of keypoint location maps m_1, \dots, m_{N_k} , where $N_k = 6$ is the total number of predefined semantic keypoints.

The network architecture was selected through experimentation. We tried 2 different architectures:

- The convolutional pose machines (CPM) [22] architecture, whose task of human pose estimation through keypoint localization closely resembles our own, and
- ResNet-50 [10], a general purpose network with high performance on a number of image understanding tasks, such as object detection and semantic segmentation.

In both cases, we trained the network using an L2 loss function on the difference between the output and ground truth keypoint location maps.

Perhaps surprisingly, ResNet-50 resulted in the highest test accuracy (see Table 1). Although the task that CPM was meant for (keypoint detection) more closely resembles our own, it cannot compete with the fact that ResNet-50 was pretrained on ImageNet, the data distribution of which is more similar to ours.

We employed the TensorFlow implementation of ResNet-50. By using an input image size of 512×512 and a bottleneck stride of 8 we get a final keypoint map size of $r = 64$. The full architecture can be seen in Table 2. The training data we used is discussed in Section 4.8.

4.3 Candidate generation

Now that the camera parameters and keypoint locations have been estimated, we move on to the candidate generation stage. In this part, predefined object templates are fit to different subsets of the estimated keypoint locations, and scored by their agreement with the entire keypoint map. First, we will describe how we get specific keypoint locations from the estimated keypoint maps. Then, we will discuss how we construct the object templates from our set of 3D models. Finally, we describe the actual candidate generation process.

4.3.1 Keypoint locations from keypoint location maps

The keypoint estimation network’s output consists of N_k single channel keypoint location maps m_1, \dots, m_{N_k} . For our candidate generation process, these maps need to be

layer name	output size	node type
input	512 × 512	
conv_1	256 × 256	7 × 7, stride 2
max_pool	128 × 128	Max pooling, stride 2
block_1	64 × 64	Bottleneck units with shortcuts, $\begin{bmatrix} 1 \times 1, 64 \\ 3 \times 3, 64 \\ 1 \times 1, 256 \end{bmatrix} \times 3$, last 3 × 3 stride 2
block_2	64 × 64	Bottleneck units with shortcuts, $\begin{bmatrix} 1 \times 1, 128 \\ 3 \times 3, 128 \\ 1 \times 1, 512 \end{bmatrix} \times 4$, all stride 1
block_3	64 × 64	Bottleneck units with shortcuts, $\begin{bmatrix} 1 \times 1, 256 \\ 3 \times 3, 256 \\ 1 \times 1, 1024 \end{bmatrix} \times 6$, all stride 1
block_4	64 × 64	Bottleneck units with shortcuts, $\begin{bmatrix} 1 \times 1, 512 \\ 3 \times 3, 512 \\ 1 \times 1, 2048 \end{bmatrix} \times 3$, all stride 1

Table 2: ResNet-50 based architecture used for keypoint estimation.

converted to concrete keypoint locations. We cannot simply take all locations with a value above a certain threshold, as the maps spread the probability of a found keypoint across multiple pixels (Figure 8). One way of dealing with this is to find all local maxima in each map. The issue with this is that large regions of very low probability still have many local maxima. To discount these, we first pass each map m_i through a thresholding operation with threshold τ_m , discarding all pixels below that value. Then, we find all 8-neighbourhood local maxima in each map m_i , and store them as our candidate keypoint locations. We denote the found keypoint locations of type k as Q_k , and the full set $Q = \{Q_1, \dots, Q_{N_k}\}$. See Figure 9.



Figure 9: Keypoint candidate locations are found by thresholding the output of the neural network and then finding local maxima

4.3.2 Object templates

From the keypoint candidates Q , we want to find actual chair candidates. As all chairs are slightly different in shape, and fitting each chair model in our dataset individually is prohibitively expensive, we make use of a chair template model.

Specifically, we create this chair template model by fitting a Principal Component Analysis (PCA) basis to the 3D coordinates of all 8 keypoints of all chair models in our database M . By analysing the cumulative percentage of variance of each resulting PCA dimension, we conclude that the top 3 PCA dimensions are responsible for $> 85\%$ of variance in the shape of all chairs. These top 3 PCA dimensions represent our chair template model T , and the deviation from the mean $p \in \mathbb{R}^3$ represents a variable for our optimization. See Figure 10.

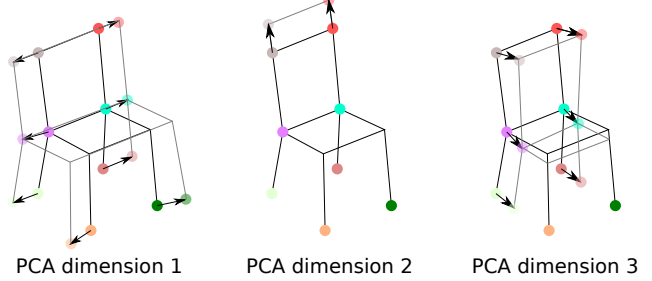


Figure 10: Visualization of the top 3 PCA dimensions of our chair template, with respect to the mean chair. They approximately correspond to respectively chair width, back height and chair depth.

We define $T(p)$ as the reprojection of PCA parameters p to 3D world space, i.e. the instantiated coordinates of one particular instance of the chair template.

4.3.3 Candidate keypoint sets

Finally, we will fit the generated chair template T to the found keypoint locations Q . Unfortunately, we do not have any correspondences between the keypoint locations of different types – for example, we do not know which “top-left” keypoint belongs with which “front-right-leg” keypoint. As such, we generate the exhaustive set of candidates by fitting a candidate chair placement to each minimum set of 2D keypoint locations that results in a well-defined fitting problem. A single keypoint correspondence is not enough, as any candidate placement can then be rotated around its up-axis indiscriminately. As we know the camera and thus the ground plane, and work under the assumption that the chair models can change only scale and azimuth (i.e. are placed flat on the ground), we can suffice with 2 keypoint correspondences. Although this does leave some ambiguities due to overlap between the scale dimension and the template parameters, due to regularization on both of these parameter sets the resulting problem is well-defined. We thus create our set of 2D keypoint candidate pairs as

$$K = \bigcup_{Q_i \in Q} \bigcup_{Q_j \in Q \setminus Q_i} Q_i \times Q_j,$$

where \times represents the Cartesian product.

4.3.4 Template fitting

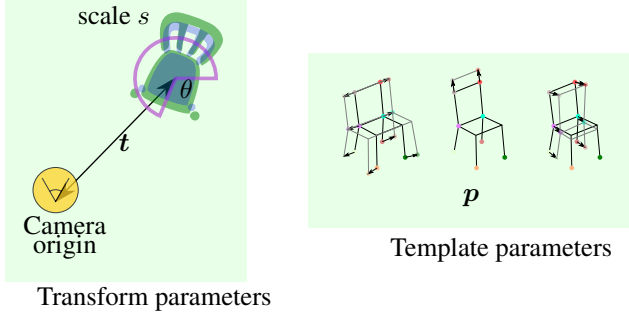


Figure 11: Parameters estimated during the candidate fitting process.

Then, we will generate one candidate chair placement for each $K_i \in K$ by finding the optimal parameters that yield a reprojection of the template’s keypoints in line with K_i , as well as the full keypoint location maps m . These parameters consist of:

- a 2D translation across the ground plane t ,
- 1D azimuth θ ,
- 1D scale s ,
- 3D chair template parameters p .

See Figure 11 for clarification. This optimization is split into two stages. In the first stage, we will optimize specifically for the reprojection of the 3D keypoints corresponding to $k_u, k_v \in K_i$. In the second stage, we will incorporate our knowledge of the other keypoint location maps in m and further finetune the parameters to match with them as closely as possible as well. We now describe each stage in turn.

First stage – optimization w.r.t. 2 keypoints In the first stage, we find the optimal parameters such that the reprojection of the chair template’s keypoints line up with K_i . We define the reprojection z_i of each keypoint $k_i, i \in \{u, v\}$ as

$$z_i = P(R(s[T(t)]_i, \theta) + t, C),$$

where R represents rotation, and P represents camera projection.

The objective function is then simply the summed mean squared error of these reprojections w.r.t. the data:

$$L = \sum_{i \in \{u, v\}} \|z_i - k_i\|^2$$

We initialize the parameters as $t = \mathbf{0}, \theta = 0, s = 1, p = \mathbf{0}$. Furthermore, we add an L2 regularization term to both the norm of the template parameters p as well as the scale s . This non-linear least squares optimization problem is then solved using Ceres [3].

Second stage – optimization w.r.t. all keypoints Now that the parameters have been optimized w.r.t. our keypoint pair K_i , we finetune the parameters by also taking into account the other keypoint location maps in m . Note that we now go back to using the keypoint location maps themselves instead of the extracted local maxima – we do not optimize for exact location anymore, and allow the final reprojection to deviate from the maxima in each individual keypoint location map. Instead, we maximize the *total probability* over all keypoint location maps. Our objective function thus becomes:

$$L = \sum_{i \in \{1, \dots, N_k\}} \|1 - m_i(z_i)\|^2,$$

where $m_i(z_i)$ represents the value of keypoint location map m_i at reprojected keypoint z_i . The same L2 regularizations as in the first stage apply, and we again solve our problem using Ceres [3].

If the final loss of the second stage is lower than a threshold τ_u we add the final parameters as a candidate placement to our candidate placement set O . This candidate placement set is then passed on to the candidate selection stage.

4.4 Candidate selection

In the final stage of our pipeline, we incorporate the key insight of this method, as discussed in the introduction, which states that we need to use higher level scene statistics to maximize our mockup performance. Specifically, we take the candidate placements O from the previous stage and employ a combination of the keypoint location maps and a model of object co-occurrence statistics to select the final subset of chairs that constitutes our scene mockup.

4.4.1 Scene statistics

To model these higher level scene statistics, we employ a pairwise object co-occurrence model. It models the probability of two chairs occurring at a given relative orientation and translation from each other. To create this model, we fit a Gaussian Mixture Model over the relative orientation δ_θ and translation δ_t of pairs of chairs in the synthetic scene dataset PBRS (see Section 4.8). We only take into account chairs that are within a distance $\delta_r = 1.5m$ from each other, reasoning that chairs that are farther apart are more likely to belong to entirely different groups of chairs, making it imprudent to base our reconstruction on their relationship. See Figure 12 for clarification.

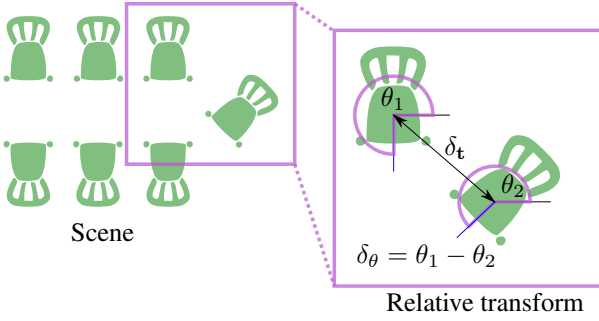


Figure 12: We extract relative transformations of pairs of chairs from the PBRS dataset and fit a GMM to these data-points.

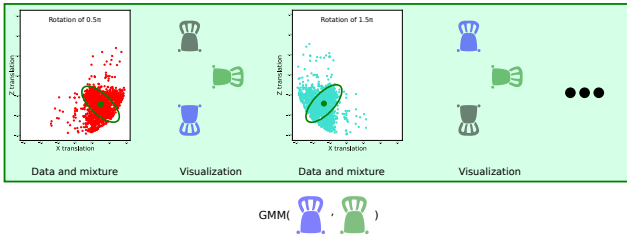


Figure 13: A visualization of two of the mixture components resulting from fitting the GMM to the relative transformations of pairs of chairs in the PBRS dataset. The means and standard deviational ellipses are plotted in green.

Fitting the GMM was done using Expectation-Maximization. As the models in PBRS tend to be aligned exactly, we regularize the resulting mixture model by adding a small bias (0.01) to the diagonal of the fitted covariance matrices. The number of mixture components N_m was found by experimentation, and was set to 5. A visualization of some of the resulting mixture components can be found in Figure 13.

4.4.2 Graph optimization

We now need to prune our over-complete set of candidate placements using the trained object co-occurrence model. We represent this task as a graph labeling problem. Each candidate placement represents a node in the graph, and takes on a binary label representing whether or not that candidate placement is present in the final mockup. Unary costs for each label stem from the keypoint location maps, and pairwise costs stem from the scene statistics GMM. See Figure 14.

Unary cost To compute the unary score of a candidate placement $o_i \in \mathcal{O}$, we generate the keypoint location map \mathbf{n} of o_i (in the same way we would do for creating a ground

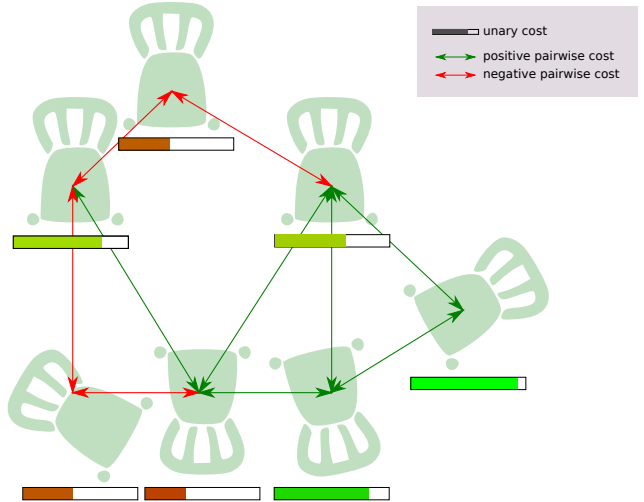


Figure 14: We model our candidate selection problem as a graph labeling problem, where the unary costs are based on the keypoint location maps, and the pairwise costs on the scene statistics GMM.

truth keypoint map) and compare it with the keypoint location map \mathbf{m} of the input image x . As we do not expect a single placement to explain the entire keypoint location map, we setup the score as a multiplicative one, with the value only being dependent on the agreement of the actual keypoints the placement o_i exhibits:

$$u_i = \frac{\|\mathbf{n} \odot \mathbf{m}\|_F}{\mathbf{n} \odot \mathbf{m}},$$

where $\|\cdot\|_F$ represents the Frobenius norm, and \odot represents the Hadamard product.

The normalization factor ensures that a candidate that perfectly matches the keypoint location map of our input image x gets a score of 1. Finally, for a specific candidate $o_i \in \mathcal{O}$, interpreting u_i as a probability we get unary costs based on the log odds of u_i :

$$U_i(0) = 0 \quad (1)$$

$$U_i(1) = -\log\left(\frac{u_i^\alpha}{1 - u_i^\alpha}\right) \quad (2)$$

where α is a scaling parameter to set the sensitivity of optimization to the value in the keypoint maps. Our choice for the log odds means that a (scaled) score of higher than 0.5 results in a candidate unary cost that *decreases* the score of the total cost when selected, and otherwise *increases* it.

Pairwise cost The pairwise cost is based entirely on the fitted GMM. We extract the relative translation δ_t and orientation δ_θ , and evaluate the trained GMM to get our raw pairwise score:

$$p_{ij} = GMM(o_i, o_j)$$

The final pairwise score is then again based on the log odds corresponding to p_{ij} . It only applies when two objects co-occur:

$$P_{ij}(0, 0) = P_{ij}(1, 0) = P_{ij}(0, 1) = 0 \quad (3)$$

$$P_{ij}(1, 1) = -\log\left(\frac{p_{ij}^\beta}{1 - p_{ij}^\beta}\right) \quad (4)$$

with β a scaling parameter similar to α .

Finally, we add an infinite pairwise cost to all candidate placement pairs that intersect. These intersections are pre-computed based on triangle-triangle intersections.

We solve the final problem setup using OpenGM [4] by converting it to a linear program and feeding it to CPLEX [2].

4.5. Iterative optimization

After the optimization from Section 4.4 is complete, we could stop and pass on the candidate placements with label 1 to the model selection stage (Section 4.6). However, now that some objects have been definitely placed, we can use this information to improve our candidate generation step, and by extension our candidate selection step. In other words, we iterate the process of candidate generation and selection, using the newly selected candidates in each iteration as a strong prior for the candidate generation process of the next generation.

4.5.1 Added pairwise cost in generation step

To take into account the already selected placements during the candidate generation phase, we keep our original non-linear least squares optimization, but to the loss function of each stage of the two stage process (see Section 4.3.4) we add a term that represents the GMM. Incorporating all mixture components in this term is hard, as it is challenging to define a well-behaved objective function to minimize that represents them. As noted by Olson et al. [18], the structure of the negative log-likelihood (NLL) of a GMM does not lend itself to non-linear least squares optimization. Instead, they propose to approximate the NLL of the full GMM by considering it as a Max-Mixture, reducing the NLL to the weighted distance to the closest mixture mean (see Figure 15 and [18] for details). In fact, in our case it makes sense to only optimize with respect to the closest mean, and not all means: a chair should either be encouraged to be next to another chair, or opposite, but never both. This replaces the original GMM likelihood function

$$p_{\text{GMM}}(\delta) = \sum_i w_i N(\mu_i, \Sigma_i)$$

with the Max-Mixture likelihood function

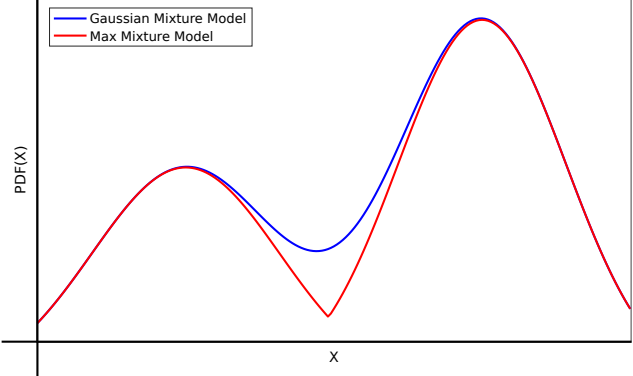


Figure 15: We approximate the GMM using a Max-Mixture Model from Olson et al., 2013 [18]. Due to the simplified negative log likelihood of this model we can then use it in our non-linear least squares optimization.

$$p_{\text{Max}}(\delta) = \max_i w_i N(\mu_i, \Sigma_i),$$

where $\delta = \begin{bmatrix} \delta_t \\ \delta_\theta \end{bmatrix}$ is the relative translation and orientation of the new candidate w.r.t. the already placed object, and w_k is the weight of the k th mixture in the model.

Taking the negative log likelihood gives

$$-\log(p_{\text{Max}}(\delta)) = \min_k \frac{1}{2} (\delta - \mu_k)^T \Sigma_k^{-1} (\delta - \mu_k) - \log(w_k \eta_k),$$

where $N(\mu, \Sigma)$ represents the normal distribution, and η_k is the Gaussian normalization factor for the k th mixture. At optimization time, during each step we find the mixture component k^* that minimizes this function, and then optimize w.r.t. the negative log likelihood of the Gaussian of that component alone, resulting in the following term to be added to the objective function:

$$\frac{1}{2} (\delta - \mu_{k^*})^T \Sigma_{k^*}^{-1} (\delta - \mu_{k^*})$$

By decoupling the component selection from the optimization step, we've restored the nice properties of the single Gaussian negative log likelihood. This term is added for each already placed object.

4.5.2 Added unary cost in selection step

As the already selected placements are not part of the optimization during later iterations, the influence of the GMM on a new candidate placement w.r.t. already selected placements becomes a unary cost. So, for each candidate placement in the second iteration, we add a term to $U_i(1)$ w.r.t. each of the already selected placements:

Name	Description	Value
α	Sensitivity of keypoint maps	0.61
β	Sensitivity to object co-occurrence model	0.14
τ_m	Lower threshold of keypoint location map	0.25
τ_u	Maximum cost for selecting candidate	0.21

Table 3: Hyper parameters of optimization, found by HyperOpt [12]

$$-\log\left(\frac{GMM(o_i, o_j^*)^\beta}{1 - GMM(o_i, o_j^*)^\beta}\right)$$

With these modifications, the candidate generation step and candidate selection step are iterated until convergence, i.e. until no new objects are added to the scene.

4.6. Model selection

The set of all selected placements still only consist of template parameters, not actual chair models. As a final step, we find the chair g^* in our database M that best fits the template. To do so, we reproject the 3D keypoint coordinates of each chair in the database to the PCA coordinate space, and find the chair whose PCA coordinates are closest to the PCA coordinates of our template:

$$g^* = \arg \min_{g \in M} \|[\text{PCA}(g)]_0^3 - p\|^2,$$

where p are the PCA coordinates of the candidate’s template.

The resulting chair models together with their transform constitute our final scene mockup.

4.7. Hyper parameters

Our optimization pipeline depends on a number of hyper parameters. We optimized these using HyperOpt [12], which employs a Tree of Parzen Estimators (Bergstra et al., 2013 [6]). As our objective function we used the PercCorrectFull measure (see Section 5.2). As ground truth data we used 10 scenes we annotated specifically for this purpose, in the same way as the data used for evaluation (see Section 5.1). See Table 3 for a list of resulting hyper parameter values.

4.8. Data

4.8.1 Image data

For purposes of qualitative evaluation, we scraped the interior design website [1] for the top 1000 results of the search query “dining room”. We denote this dataset HOUZZ. These images are high quality and represent difficult but fair scenarios on which we expect our method to perform well. Some examples of these images can be seen in Figure 16.



Figure 16: Example images from our scraped HOUZZ dataset.

4.8.2 Network training data

Traditionally, training a deep neural network requires a large amount of training data. To our knowledge, there is no known large dataset of photographs accurately annotated with object keypoints. As such, we resort to creating our own training data. Ideally, the training data should be from the same distribution as our intended testing data, i.e. photographs of indoor scenes. However, creating a large-scale dataset of this type is extremely time-consuming and expensive. On the other hand, synthetic data in the form of realistic 3D indoor scenes along with physically-based renders is already available in high numbers [24]. Still, despite the high quality of the renders, there is still a significant discrepancy between the feature distribution of the renders and that of the photographs. As such, we augment the synthetic dataset with a subset of real photographs from HOUZZ annotated through Amazon Mechanical Turk. We now discuss each data type in turn.

Synthetic data The dataset provided by Zhang et al. [24] provides 45K realistic indoor scenes, and 400K physically-based renders of these scenes (see Figure 17). We denote this dataset as PBRs. These scenes consist of a fixed set of 2500 different models across 60 classes. Among these models there are ± 250 chairs. We took a subset of 100 of these chairs and annotated them with our previously selected keypoint types. We then took all renders that contain at least 1 of the annotated chairs and reprojected the keypoint locations into these renders, yielding one image/keypoint map pair as training data per render. This resulted in a set of ± 8000 image/keypoint map pairs in total.

Real data Unfortunately, the synthetic data alone does not result in good performance on real data. Two distinct reasons can be identified. First, even though the renders in PBRs are of high quality, their feature distribution is both distinct from real photographs as well as less diverse. Secondly, at the time of writing, the set of renders and the set of scenes available for PBRs had some discrepancies between them, resulting in a small but significant set of renders that do not agree with the automatically generated keypoint maps.

To address both of these issues, we annotated a subset of

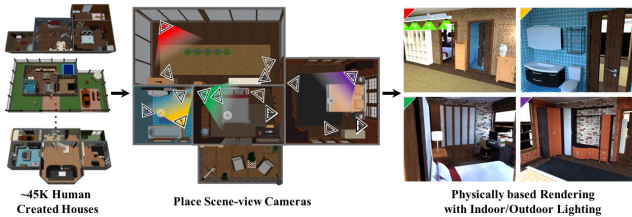


Figure 17: For the training setup of our network with synthetic data, we use renders from the PBRS dataset [24], which provides $\pm 45\text{K}$ houses with $\pm 400\text{K}$ high quality renders. Figure from [24].

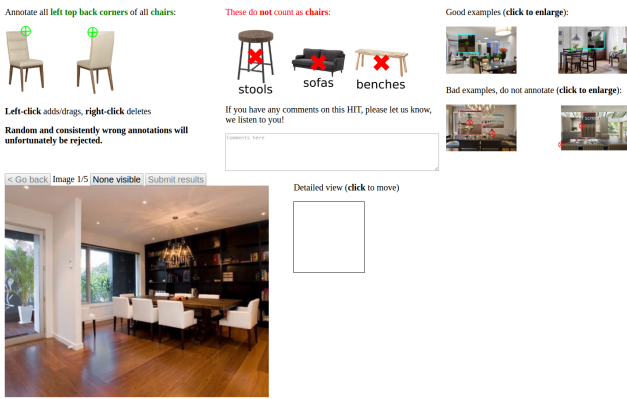


Figure 18: The Amazon MTurk interface we used to annotate 500 photographs with keypoints.

500 images from the HOUZZ dataset through Amazon Mechanical Turk. We asked 3 workers per image to annotate all keypoints in the image through a drag-and-drop interface (see Figure 18), and averaged the resulting 3 keypoint maps per image. This resulted in a training set of 500 hand-annotated photographs, which was then used to train our keypoint estimation network.

Final training set We experimented with 3 different training setups. In the first setup, we trained the network only with synthetic data. In the second setup, we only trained the network with real data. Finally, in the third setup, we first trained the network until convergence with the synthetic data, and then finetuned the network using the smaller set of real data.

Surprisingly, the best performance on the test set resulted from setup 2, i.e. training only with the real data. Apparently, the shortcomings of the synthetic data mentioned above were of higher importance than expected. One likely explanation is the fact that training the network with the synthetic data first steers away the network weights from those that were the result of the ImageNet pretraining, which already encompass a high general understanding

of real photographs. The numbers show that this initial information is more valuable than the extent of the synthetic data as well as its structural similarity to our test data.

4.8.3 Model data

The models annotated for the purpose of generating synthetic network training data also immediately function as our model set M .

5. Evaluation

We thoroughly evaluated our method, investigating the importance of each part of our pipeline as well as comparing our results with other methods. We will first discuss the creation of a set of ground truth annotated scenes for the purpose of quantitative evaluation (Section 5.1). We then define a set of diverse performance measures (Section 5.2), after which we introduce two baseline methods for comparison purposes (Section 5.3). We evaluate our method with the ground truth set, and compare the numbers with two distinct baseline methods (Section 5.4). Finally, we perform an ablation study to show the influence of each on the final performance (Section 5.5). Both quantitative and qualitative results will be shown along the way.

5.1. Ground truth annotation

In order to quantitatively measure the performance of both the baseline methods and our own, we need a set of ground truth annotated scenes, i.e. images for which all objects have been placed manually. We setup an application in which an object can be placed by clicking and dragging, as well as by annotating a number of keypoints of the object and optimizing for its location and scale. Moreover, objects can be copied and translated along their local coordinate axes, allowing for quick and precise annotation (see Figure 19). We use the automatically estimated camera parameters, making sure we discard any scenes for which the camera estimation is completely off. We used this tool to fully annotate 100 scenes, which were randomly selected from our HOUZZ dataset of 1000 images.

5.2. Performance measures

A scene mockup method can be quantitatively evaluated in many different ways. As no single measure tells the full story, we have opted for a number of different ones.

Notation We will use the concept of “source” and “target” to denote the two scenes between which some measure is computed. We specifically do not use “result scene” and “ground truth scene”, because they can act as either source or target scene in most measures. We denote the objects in the source and target scene as $o_S \in \mathcal{S}$, $o_T \in \mathcal{T}$ respectively. $J_3(o_S, o_T)$ and $J_2(o_S, o_T)$ represent the Jaccard index or



Figure 19: We created a ground truth annotation tool for quickly creating ground truth scene mockup examples.

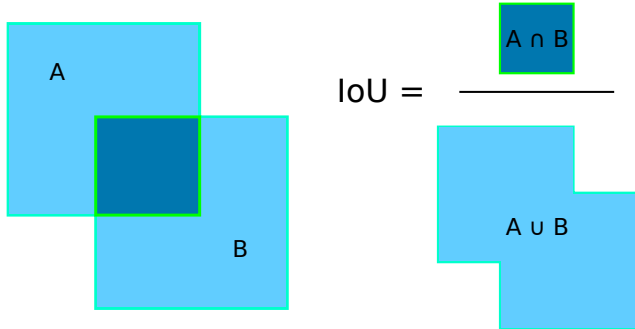


Figure 20: Visualization of the intersection-over-union measure in 2D.

intersection-over-union (IoU) of the bounding boxes of o_S and o_T in 3D world space and 2D screen space respectively (see Figure 20). Finally, given an object o_S we define the “ J_i^* correspondence” with \mathbf{T} as the object in T with the maximum Jaccard index with o_S :

$$J_i^*(o_S, \mathbf{T}) = \arg \max_{o_T \in \mathbf{T}} J_i(o_S, o_T)$$

Intuitively, this returns, for a given object, the ”best matching” object from the other scene in terms of overlap.

Average Max IoU This measure takes a source scene and a target scene, and records the accuracy with which the volumes of the objects in the source scene agree with the objects in the target scene. Specifically, for each object in the source scene, we record the IoU of the object with its MaxIoU correspondence. This measure is averaged over all objects in the source scene to produce the final measure.

$$\text{AvgMaxIoU}(\mathbf{S}, \mathbf{T}) = \frac{1}{|\mathbf{S}|} \sum_{o_S \in \mathbf{S}} J_3(o_S, J_3^*(o_S, \mathbf{T}))$$

We measure in both directions, i.e. with the ground truth as source and result as target, as well as vice versa. The former can be thought of as a form of “recall” and the latter as a form of “precision”. This measure is angle-agnostic and captures the location similarity of objects in the source scene w.r.t. those in the target scene.

Percentage correct location This measure takes a source scene and a target scene, and records the percentage of objects in the source scene that have a J_3^* correspondence over a certain threshold τ_J . To define it, we first set

$$\begin{aligned} \text{CorrectLoc}(\mathbf{S}, \mathbf{T}) &= \\ \{o_S \in \mathbf{S} \mid J_3(o_S, J_3^*(o_S, \mathbf{T})) > \tau_J\}. \end{aligned}$$

Then,

$$\text{PercCorrectLoc}(\mathbf{S}, \mathbf{T}) = \frac{|\text{CorrectLoc}(\mathbf{S}, \mathbf{T})|}{|\mathbf{S}|}.$$

We again measure in both directions, yielding recall (ground truth is source, result is target) and precision (vice versa) measures.

Percentage correct As the previous measure, but with the added constraint that the angle difference is under a threshold τ_θ . So,

$$\begin{aligned} \text{CorrectFull}(\mathbf{S}, \mathbf{T}) &= \\ \{o_S \in \text{CorrectLoc}(\mathbf{S}, \mathbf{T}) \mid \angle(o_S, J_3^*(o_S, \mathbf{T})) < \tau_\theta\}. \end{aligned}$$

Then,

$$\text{PercCorrectFull}(\mathbf{S}, \mathbf{T}) = \frac{|\text{CorrectFull}(\mathbf{S}, \mathbf{T})|}{|\mathbf{S}|}.$$

Angle difference This measures the average angle difference for the objects that have correct location. This measure is symmetrical.

$$\begin{aligned} \text{AngleDiff}(\mathbf{S}, \mathbf{T}) &= \\ \frac{\sum_{o_S \in \text{CorrectLoc}(\mathbf{S}, \mathbf{T})} \angle(o_S, J_3^*(o_S, \mathbf{T}))}{|\text{CorrectLoc}(\mathbf{S}, \mathbf{T})|} \end{aligned}$$

Average Max 2D IoU This measures the average maximum IoU of the bounding boxes of each projected object in the source scene with the bounding boxes of the projected objects in the target scene.

$$\text{AvgMax2DIoU}(\mathbf{S}, \mathbf{T}) = \frac{1}{|\mathbf{S}|} \sum_{o_S \in \mathbf{S}} J_2(o_S, J_2^*(o_S, \mathbf{T}))$$

5.3. Baseline methods

We compare our method with two baselines from the literature. As the exact problem formulation we employ has to our knowledge not been attempted, we convert the output of each baseline (in both cases 3D pose but 2D, image space locations of chairs) to the 3D scene mockup format that our method produces.

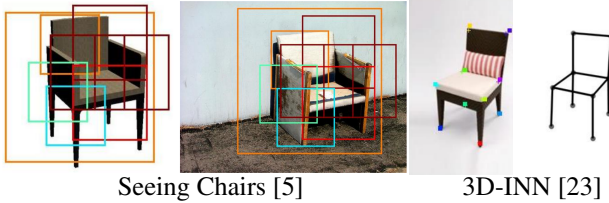


Figure 21: Example of raw output of the two baseline methods.

Seeing chairs [5] This method from Aubry et al. finds chairs by matching so-called “discriminative visual elements” or DVEs from a set of rendered views of 1000+ chair models with the input image. These DVEs are linear classifiers over HOG features [7] learnt from the rendered views in a discriminative fashion. They are learned at multiple scales, and only the most discriminative ones are kept for matching purposes. At test time, a patch-wise matching process finds the best-matching image patch/rendered patch pairs, and then finds sets of pairs that come from the same rendered view (see Aubry et al.’s paper for details [5]).

This method outputs scored image space bounding boxes together with a specific chair model and pose. See Figure 21, left. For the 3D performance measures (Section 5.2) we need the output in the form of a 3D scene. To this end we convert each set of bounding box, pose, and chair model to a 3D scene. As the camera is known (Section 4.1), we can optimize the location (in the X-Z plane) of the 3D model without changing its pose, such that the 2D bounding box of the projected model matches as closely as possible with the detected bounding box. This can be formulated as a least-squares optimization problem, which we solve using Ceres [3].

FasterRCNN [19] + 3D-INN [23] This baseline is a combination of a convolutional neural network (CNN) trained for object detection (FasterRCNN) and another CNN trained for 3D object interpretation (3D-INN). We use FasterRCNN to extract bounding boxes of chairs from the input image, and then feed these regions of interest to 3D-INN, which produces a templated chair model consisting of a set of predefined 3D keypoints as well as a pose estimate (azimuth and elevation). See Figure 21, right. The set of keypoint types we have chosen for our method is a subset of

the keypoints produced by 3D-INN, and thus we can use the candidate generation part of our pipeline (see Section 4.3) to convert the extracted keypoints to a 3D chair.

5.4. Comparison

We ran our pipeline and the two baseline methods on the full ground truth annotated scene set (Section 5.1). A sampling of results can be seen in Figure 22. The same visualization for all 100 scenes in our ground truth set can be found in Appendix ??.

The baseline methods perform well when there is no occlusion in the scene. Chairs that are clearly visible are reconstructed reliably, as the visual information directly available is enough for these methods to make a reasonable inference about the object’s pose and identity. However, when a chair is partly occluded, these methods break down quickly. In contrast, our method is more often able to recover from these situations, due to the incorporation of the object co-occurrence model.

This difference in performance is also reflected in the quantitative results. We extracted the performance measures listed in Section 5.2 from each method, and list them in Table 4. Our method outperforms the baselines on all counts. Moreover, in Figure 23 we show how the PercCorrectFull measure changes under varying thresholds of IoU and angle (see Section 5.2).

5.5. Ablation study

Finally, we evaluated the importance of each of our pipeline’s optional steps to the final performance. Specifically, we ran our pipeline on the full test set under two weakening conditions. In the first condition, we disable all pairwise costs, and run the entire pipeline based solely on the keypoint location maps. In the second condition, we only run the second and third stage once, removing the possibility of the candidate generation stage benefiting from previously placed objects. Results are found in Table 5.

There are some things to note. First, although AvgMaxIOU recall increases when disabling scene statistics, the precision goes down significantly. This makes sense, as the pairwise costs by themselves do not propose new objects – they only make output mockups more precise by pruning objects that do not agree with others. Second, using only a single iteration increases precision, but recall takes a significant hit. Again, this is logical, as in later iterations the keypoint location maps have decreased influence relative to the pairwise costs. This means that objects with weaker keypoint response get found more easily, but also that false positives are somewhat more likely. Overall, the combined AvgMaxIOU F1 measure is highest for the full pipeline, and perhaps most importantly the PercCorrectFull F1 measure as well.

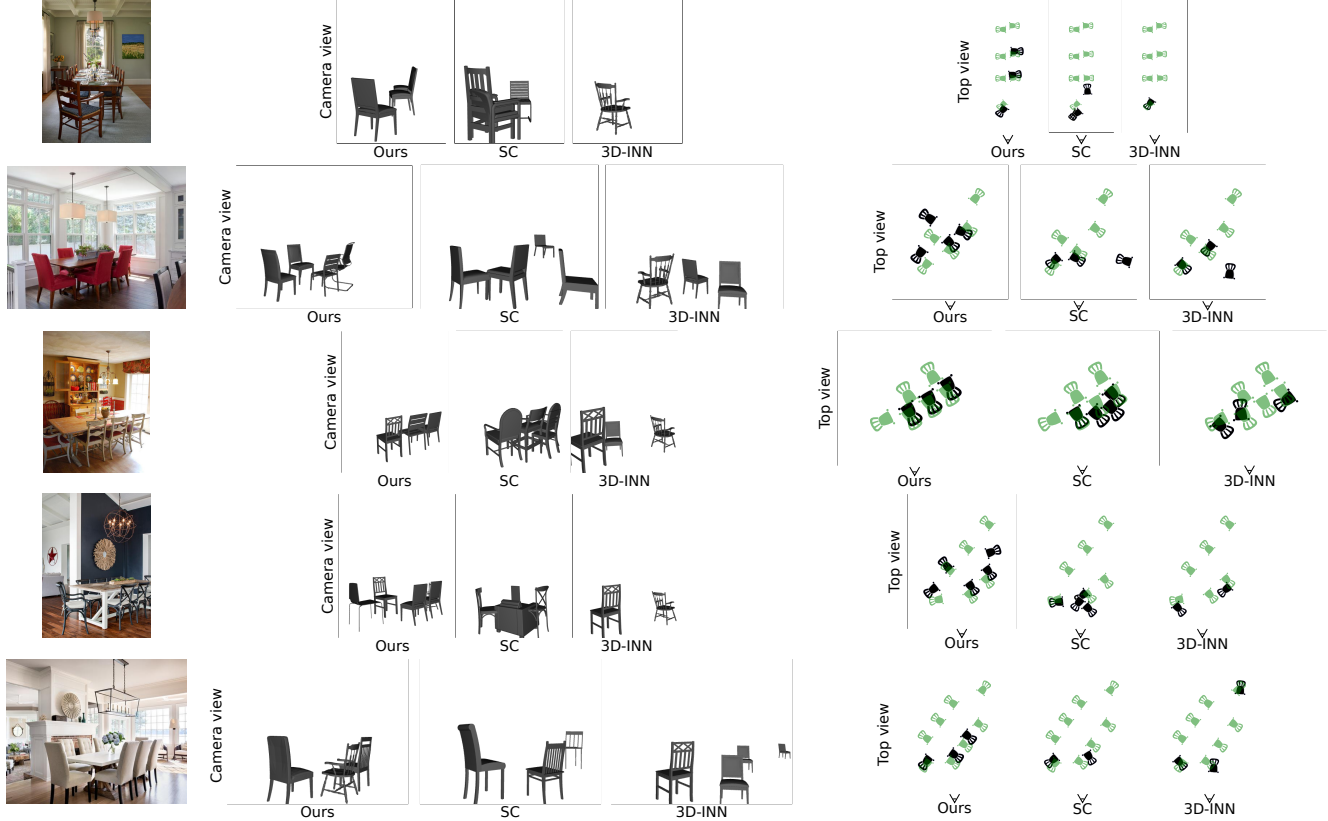


Figure 22: Qualitative results for our method vs. the baseline methods.

	AvgMaxIoU (precision)	AvgMaxIoU (recall)	AvgMaxIoU (F1)	
3D-INN [23] + FasterRCNN [19]	0.316	0.150	0.198	
SeeingChairs [5]	0.195	0.128	0.149	
Ours	0.386	0.250	0.293	
	PercCorrect (precision)	PercCorrect (recall)	PercCorrect (F1)	
3D-INN [23] + FasterRCNN [19]	0.263	0.124	0.165	
SeeingChairs [5]	0.071	0.043	0.052	
Ours	0.298	0.167	0.207	
	PercCorrectFull (precision)	PercCorrectFull (recall)	PercCorrectFull (F1)	
3D-INN [23] + FasterRCNN [19]	0.04	0.015	0.021	
SeeingChairs [5]	0.013	0.007	0.009	
Ours	0.285	0.161	0.198	
	AvgMax2DIoU (precision)	AvgMax2DIoU (recall)	AvgMax2DIoU (F1)	AngleDiff (in degrees)
3D-INN [23] + FasterRCNN [19]	0.526	0.336	0.401	55.8
SeeingChairs [5]	0.372	0.325	0.341	11.4
Ours	0.628	0.470	0.525	7.3

Table 4: Quantitative performance of our method vs. the two baseline methods. We outperform the baseline significantly across all measures.

6. Discussion

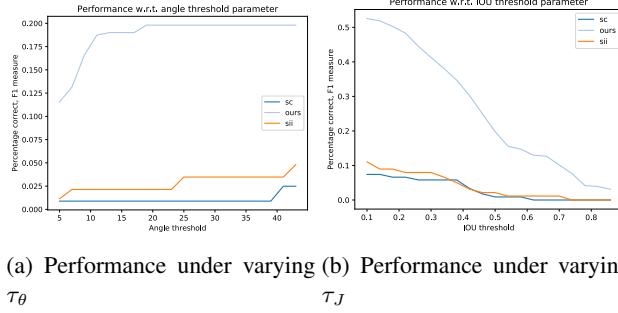
We proposed a method for automatically finding chairs in a photograph of a structured scene. Our key insight which gives us an advantage over other methods is the incorporation of higher level scene statistics, allowing us to rea-

son more accurately about objects that are highly occluded. Through quantitative and qualitative evaluation, we have shown a considerable increase in performance across multiple measures. Nevertheless, some limitations of our method remain:

- Our method is currently only suited to chairs. How-

	AvgMaxIOU (precision)	AvgMaxIOU (recall)	AvgMaxIOU (F1)	PercCorrectFull (precision)	PercCorrectFull (recall)	PercCorrectFull (F1)
Full pipeline	0.386	0.250	0.293	0.285	0.161	0.198
No scene stats	0.296	0.265	0.267	0.174	0.151	0.154
Single iteration	0.421	0.190	0.251	0.346	0.123	0.175

Table 5: Ablation study showing the importance of using scene statistics and multiple iterations for best performance.



(a) Performance under varying (b) Performance under varying

θ_θ

τ_J

Figure 23: Changes in performance under varied angle and IoU thresholds.

ever, this is not a limitation of the method, and with a proper data annotation effort it could be extended to arbitrary other classes. Note that adding more classes will likely improve the accuracy of finding chairs by themselves as well, as there will be more scene information to draw from.

- The keypoint network is currently trained with 500 sample images. This is a very small set of data, and the performance of the network has clear room for improvement through the addition of more training data. However, gathering such data is expensive. Finding a better way to incorporate large amounts of synthetic training data into the pipeline is an interesting avenue for future work.
- After candidate selection, we do not reoptimize the position and orientation of each object. As we now have the added information of the location of the other objects, this could result in more accurate object placements.
- We do not explicitly model style. Although the use of the chair template does have some influence on the outer shape of the chair being used, there are many more properties that could be modelled for a more convincing mockup.

References

- [1] houzz.
url`https://www.houzz.co.uk/`.
- [2] IBM ILOG CPLEX Optimizer.
url`http://www-01.ibm.com/software/integration/optimization/cplex-optimizer/`.
- [3] S. Agarwal, K. Mierle, and Others. Ceres solver. <http://ceres-solver.org>.
- [4] B. Andres, T. Beier, and J. Kappes. OpenGM: A C++ library for discrete graphical models. *CoRR*, abs/1206.0111, 2012.
- [5] M. Aubry, D. Maturana, A. A. Efros, B. C. Russell, and J. Sivic. Seeing 3d chairs: Exemplar part-based 2d-3d alignment using a large dataset of CAD models. In *Proc. Conference on Computer Vision and Pattern Recognition*, pages 3762–3769, 2014.
- [6] J. Bergstra, D. Yamins, and D. Cox. Making a science of model search: Hyperparameter optimization in hundreds of dimensions for vision architectures. In *Proc. International Conference on Machine Learning*, pages 115–123, 2013.
- [7] N. Dalal and B. Triggs. Histograms of oriented gradients for human detection. In *Proc. Conference on Computer Vision and Pattern Recognition*, pages 886–893, 2005.
- [8] M. Fisher, D. Ritchie, M. Savva, T. Funkhouser, and P. Hanrahan. Example-based synthesis of 3d object arrangements. *Proc. ACM/SIGGRAPH Asia*, 2012.
- [9] M. Fisher, M. Savva, Y. Li, P. Hanrahan, and M. Nießner. Activity-centric scene synthesis for functional 3d scene modeling. *Proc. ACM/SIGGRAPH*, 34(6):179, 2015.
- [10] K. He, X. Zhang, S. Ren, and J. Sun. Deep residual learning for image recognition. In *Proc. Conference on Computer Vision and Pattern Recognition*, pages 770–778, 2016.
- [11] V. Hedau, D. Hoiem, and D. A. Forsyth. Recovering the spatial layout of cluttered rooms. In *Proc. International Conference on Computer Vision*, pages 1849–1856, 2009.
- [12] HyperOpt. HyperOpt, 2017.
- [13] H. Izadinia, Q. Shan, and S. M. Seitz. IM2CAD. *CoRR*, abs/1608.05137, 2016.
- [14] Y. Li, A. Dai, L. J. Guibas, and M. Nießner. Database-assisted object retrieval for real-time 3d reconstruction. *Comput. Graph. Forum*, 34(2):435–446, 2015.
- [15] J. J. Lim, H. Pirsiavash, and A. Torralba. Parsing IKEA objects: Fine pose estimation. In *Proc. International Conference on Computer Vision*, pages 2992–2999, 2013.
- [16] O. Mattausch, D. Panozzo, C. Mura, O. Sorkine-Hornung, and R. Pajarola. Object detection and classification from large-scale cluttered indoor scans. *Comput. Graph. Forum*, 33(2):11–21, 2014.
- [17] A. Monszpart, N. Mellado, G. J. Brostow, and N. J. Mitra. Rapter: rebuilding man-made scenes with regular arrangements of planes. *Proc. ACM/SIGGRAPH*, 34(4):103, 2015.
- [18] E. Olson and P. Agarwal. Inference on networks of mixtures for robust robot mapping. *I. J. Robotics Res.*, 32(7):826–840, 2013.
- [19] S. Ren, K. He, R. B. Girshick, and J. Sun. Faster R-CNN: towards real-time object detection with region proposal networks. In *Proc. Advances in Neural Information Processing Systems*, pages 91–99, 2015.

- [20] T. Shao, A. Monszpart, Y. Zheng, B. Koo, W. Xu, K. Zhou, and N. J. Mitra. Imagining the unseen: stability-based cuboid arrangements for scene understanding. *Proc. ACM/SIGGRAPH*, 33(6):209:1–209:11, 2014.
- [21] I. Tsochantaridis, T. Joachims, T. Hofmann, and Y. Altun. Large margin methods for structured and interdependent output variables. *Journal of machine learning research*, 6(Sep):1453–1484, 2005.
- [22] S. Wei, V. Ramakrishna, T. Kanade, and Y. Sheikh. Convolutional pose machines. In *Proc. Conference on Computer Vision and Pattern Recognition*, pages 4724–4732, 2016.
- [23] J. Wu, T. Xue, J. J. Lim, Y. Tian, J. B. Tenenbaum, A. Torralba, and W. T. Freeman. Single image 3d interpreter network. In *European Conference on Computer Vision*, pages 365–382, 2016.
- [24] Y. Zhang, S. Song, E. Yumer, M. Savva, J. Lee, H. Jin, and T. A. Funkhouser. Physically-based rendering for indoor scene understanding using convolutional neural networks. In *Proc. Conference on Computer Vision and Pattern Recognition*, 2017.